

12-1-2013

Image registration of ex-vivo MRI to sparsely sectioned histology of hippocampal and neocortical temporal lobe specimens.

Maged Goubran

Cathie Crukley

Sandrine de Ribaupierre

Terence M Peters

Ali R Khan

Follow this and additional works at: <https://ir.lib.uwo.ca/robartspub>

 Part of the [Bioimaging and Biomedical Optics Commons](#)

Citation of this paper:

Goubran, Maged; Crukley, Cathie; de Ribaupierre, Sandrine; Peters, Terence M; and Khan, Ali R, "Image registration of ex-vivo MRI to sparsely sectioned histology of hippocampal and neocortical temporal lobe specimens." (2013). *Robarts Imaging Publications*. 13. <https://ir.lib.uwo.ca/robartspub/13>

Image registration of *ex-vivo* MRI to sparsely sectioned histology of hippocampal and neocortical temporal lobe specimens

Maged Goubran^{a,c}, Cathie Crukley^a, Sandrine de Ribaupierre^b, Terence M. Peters^{a,c}, Ali R. Khan^{a,*}

^a*Imaging Research Laboratories, Robarts Research Institute*

^b*Department of Clinical Neurological Sciences*

^c*Biomedical Engineering, Western University, London, Ontario, Canada*

Abstract

Intractable or drug-resistant epilepsy occurs in to 30% of epilepsy patients, with many of these patients undergoing surgical excision of the affected brain region to achieve seizure control. Recent magnetic resonance imaging (MRI) sequences and analysis techniques have the potential to detect abnormalities not identified with diagnostic MRI protocols. Prospective studies involving pre-operative imaging and collection of surgically-resected tissue provide a unique opportunity for verification and tuning of these image analysis techniques, since direct comparison can be made against histopathology, and can lead to better prediction of surgical outcomes and potentially less invasive procedures. To carry out MRI and histology comparison, spatial correspondence between the MR images and the histology images must be found. Towards this goal, a novel pipeline is presented here for bringing *ex-vivo* MRI of surgically-resected temporal lobe specimens and digital histology into spatial correspondence. The sparsely-sectioned histology images represent a challenge for 3D reconstruction which we address with a combined 3D and 2D registration algorithm that alternates between slice-based and volume-based registration with the *ex-vivo* MRI. We evaluated our registration method on specimens resected from patients undergoing anterior temporal lobectomy (N=7) and found our method to have a mean target registration error of 0.76 ± 0.66 and 0.98 ± 0.60 mm for hippocampal and neocortical specimens respectively. This work allows for the spatially-local comparison of histology with post-operative MRI and paves the way for eventual correlation with pre-operative MRI image analysis techniques.

Keywords: Image Registration, MRI, Histology, Epilepsy, Anterior Temporal Lobectomy

1. Introduction

Intractable or drug-resistant epilepsy occurs in over 30% of epilepsy patients and is commonly characterized by partial refractory seizures (Engel, 1998). When there is a localized focus, the standard of care

*Corresponding author

Email address: alikh@robarts.ca (Ali R. Khan)

4 for these patients is a surgical excision of the affected brain region in order to achieve seizure control (Engel
5 et al., 1992). Current clinical imaging protocols and surface EEG techniques of epileptogenic focus localiza-
6 tion may not be sufficient for pre-operative planning due to limited sensitivity to deeper brain structures,
7 and low resolution of source localization techniques (Smith, 2005). These limitations often necessitate inva-
8 sive electrophysiological monitoring using sub-dural strips or grid electrodes. Magnetic resonance imaging
9 (MRI) techniques such as diffusion tensor imaging (DTI), relaxometry mapping, high resolution functional
10 MRI (fMRI), voxel-based morphometry, and cortical thickness analysis can detect abnormalities not identi-
11 fied with conventional or diagnostic MRI protocols (Bernasconi et al., 2000, 2004; Bernhardt et al., 2009).
12 This is important since it has been shown that post-operative outcomes can be predicted more accurately in
13 patients where lesions can be identified (de Tisi et al., 2011; Fish et al., 1993). These techniques also have
14 the potential to improve pre-operative localization of the focus, paving the way towards less invasive proce-
15 dures and better surgical outcomes. With the plethora of MRI sequences and analysis techniques available,
16 the challenge then becomes how to verify and evaluate the sensitivity and specificity of these techniques
17 for detection of abnormal brain tissue. Prospective studies involving pre-operative imaging and collection
18 of resected tissue from surgery (Eriksson et al., 2007; Howe et al., 2010) provide a unique opportunity for
19 verification and tuning of these image analysis techniques, since direct comparison can be made against
20 high-resolution *ex-vivo* imagery, histology and immunohistochemistry. In order to carry out this verifica-
21 tion, spatial correspondence between the MR images and the tissue-derived histology images must be found,
22 which remains challenging due to the deformations involved during resection of the tissue and histological
23 processing and the difficulty of accurately registering the histology slices to the MR images. Registration
24 is the task of finding this spatial correspondence by modelling the transformations and deformations that
25 occur due to surgical resection and tissue handling. These deformations can be divided into two types:
26 those occurring during surgical resection, and those occurring during histological processing. By obtaining
27 an intermediate *ex-vivo* MRI of the tissue specimen after surgical resection, we can divide this challenging
28 registration problem into two independent sub-problems that can be tackled individually. This manuscript
29 presents methodology and validation for the latter sub-problem, that is, the registration of *ex-vivo* MRI
30 with histological slides to account for transformations due to slicing, slide mounting, and other histological
31 processing. The proposed method, based on an iterative 3D and 2D image registration scheme, does not
32 require implanted landmarks, block-face images, or serially sectioned histology images, and achieves a target
33 registration error of 0.76 mm and 0.98 mm for hippocampal and neocortical specimens respectively.

34 Histological verification of MRI is rare since tissue from surgeries or postmortem specimens are required,
35 and when available validation is not a straightforward task. A previous method has been devised to manually
36 match histopathology of temporal lobe resections to MRI using a cutting cradle to resample the MRI to the
37 orientation of histology (Eriksson et al., 2005). However no image registration was performed and only visual
38 assessment of the correspondence between the MRI and photographs of histology slices was accomplished.

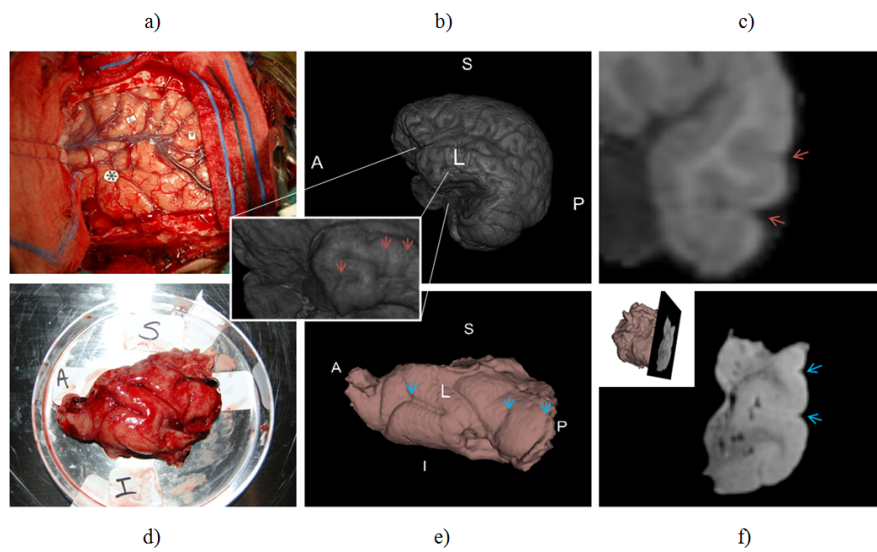


Figure 1: Example of encountered deformations. Red arrows represent cortical sulci on the pre-operative MRI and blue arrows represent the corresponding sulci on the resected neocortex specimen. a) Photograph of surgical view before resection, b) Volume rendering of a pre-operative MRI of the patient with a zoomed view showing the temporal pole, c) Coronal view of the pre-operative MRI demonstrating temporal gyri with red arrows, d) Photograph of the temporal lobe neocortex post resection, e) Surface rendering of the resected neocortex with blue arrows showing the corresponding sulci to part b), and f) Coronal view of the ex-vivo MRI with blue arrows indicating sulci corresponding to part c); the small window in the top left corner demonstrates the mesial (interior) side of the neocortex with an intersection of the shown MRI slice.

39 To evaluate the ability of high resolution MRI to resolve underlying pathologies of focal epilepsy an accurate
40 full image registration is needed as the extent of pathologies such as focal cortical dysplasia (FCD), gliosis or
41 hippocampal subfield sclerosis could be on the order of millimeters. Several challenges are met in the process
42 of finding spatial correspondence, or registration, between resected tissue and preoperative MRI. One of the
43 main challenges encountered is tissue deformation introduced due to the physical stresses experienced during
44 surgery, as well as distortions to the tissue during the histological processing. Figure 1 demonstrates such
45 tissue deformations encountered during a procedure. These deformations can be divided into primary and
46 secondary categories (Dauguet et al., 2007). Primary deformations can be thought of as three dimensional
47 changes, such as mechanical distortions during brain extraction once the resected specimen is detached
48 from surrounding brain tissue, when cutting the specimen in blocks, or non uniform shrinkage induced
49 by formalin fixation. Secondary deformations are within-slice distortions which are due to stretching of
50 microtome cut sections on a water bath, spreading histology slices over glass slides and staining. Histology
51 slices breakage, is a major manifestation of the deformations encountered during histological processing
52 of the tissue. Furthermore, differential shrinkage of the tissue is another challenge that is due to the
53 different intrinsic properties of white and grey matter. Registration of histology from surgically resected
54 brain specimen to MRI is more challenging than registration of post-mortem or animal tissue as the tissue
55 has to be sparsely sectioned, in comparison to the possibility of serially sectioning the entire specimen. This
56 is limitation is imposed by the clinical requirement of pathology departments to keep parts of the resected
57 specimen in tissue banks. The very different anatomy between sparsely sectioned adjacent histology slices
58 (several mm apart) presents itself as another significant challenge. To address the challenge of non-rigidly
59 registration 2D sparsely sectioned histology slides of brain resections from epilepsy surgery to *in-vivo* 3D
60 MRI, we propose a full image registration protocol that relies on *ex-vivo* imaging of the specimen, to enable
61 accurate correlation of histopathology with MRI. This work focuses on the intermediate registration of
62 histology images to *ex vivo* imaging of hippocampal and temporal lobe resections from anterior temporal
63 lobectomies (ATL). Our protocol reduces the complexity of the *in-vivo* MRI to histology registration problem
64 by leaving a single-modality 3D *ex-vivo* to *in-vivo* registration as the last step.

65 Presently, there are no automated histology to MRI image registration protocols that could be widely
66 applicable to focal resections of human brain, such as tissue resected during epilepsy surgery. We present
67 here a protocol to register *ex-vivo* scans of hippocampal and neocortical temporal lobe resections to histology
68 as an intermediate step that reduces the complexity of the preoperative MRI to 2D sparse histology problem.
69 Specifically we describe a novel landmark-free algorithm for simultaneous reconstruction and alignment of
70 sparsely sectioned histological data to *ex-vivo* MRI, and a quantitative validation for our registration method.
71 Performing this intermediate step addresses most of the challenges of registration to *in-vivo* imaging due to
72 the higher resolution and reduced deformations of the *ex-vivo* images. Furthermore, the higher resolution of
73 specimen imaging is advantageous for examining the correlation between MRI and histology. The proposed

74 method represents a significant step towards *in-vivo* MRI to histology registration in the clinical setting
75 and can be broadly applicable to MRI and histopathology correlations of resections other than epilepsy
76 surgery.

77 **2. Methods & Materials**

78 *2.1. Recruitment, surgery & specimen acquisition*

79 Seven patients suffering from intractable temporal lobe epilepsy (TLE) were recruited as part of an
80 ongoing study. This project has been approved by the office of research and ethics of the University of
81 Western Ontario, and informed consent was obtained from all patients prior to their recruitment in the
82 study. All such patients were recommended for ATL surgery by the department of clinical neurological
83 sciences at the University Hospital (UH) of the London Health Sciences Centre, and had preoperative
84 investigations including neuropsychological testing and 1.5T clinical MRI scans which included T1w, T2w,
85 FLAIR, and diffusion-weighted sequences. Patients were monitored with scalp-based electroencephalogram
86 (EEG) video telemetry for seizure characterization, with three patients having to undergo monitoring with
87 subdural placement of strip electrodes. In addition to the 1.5T clinical MRI scans performed at the hospital,
88 patients underwent a series of scans on 3T and 7T MRI research scanners, including high-resolution structural
89 imaging, diffusion-tensor imaging, relaxation mapping and resting-state functional imaging prior to surgery.
90 Following surgery, the resected tissue specimens were transferred to the Robarts Research Institute for
91 *ex-vivo* specimen imaging on the same 3T scanner and then to the pathology technologist for histological
92 processing. From the seven patients, fourteen resected specimens were collected, but only twelve out of the
93 fourteen were used in the study due to a fragmented hippocampus specimen and missed *ex-vivo* hippocampus
94 scan. Table 1 summarizes the patients demographic data, as well as, their clinical MRI and histopathological
95 findings.

96 *2.2. Specimen Ex-vivo MR Imaging*

97 After resection, each specimen was placed in a large petri dish within a specialized sealed cooler for
98 specimen transport, and orientation labels were marked on the container by the operating neurosurgeon,
99 with photographs taken for future reference. MR imaging was carried out on the specimens in two sessions:
100 immediately following surgical resection, and after overnight fixation in 10% formalin. For the initial session,
101 referred to as the pre-fixation session, the specimens were immediately transferred from the operating room
102 to the scanning suite at the Robarts Research Institute and prepared for imaging. Each specimen was
103 wrapped in gauze for stabilization, transferred to suitably-sized containers for imaging, and immersed in a
104 fluorine-based lubricant ‘Christo-lube’ (Lubrication Technology, Inc) prior to imaging to avoid susceptibility
105 artifacts at the tissue boundaries. Identical preparation was performed for the second post-fixation session.

| Patient | Gender | Age | Onset age | Seizure origin | MRI | Path. | Scan Protocol |
|---------|--------|-----|-----------|----------------|--------------------|-----------------|---------------|
| 1 | F | 51 | 10 | Right | Normal | dysplasia | I |
| 2 | F | 22 | 15 | Right | Normal | mild MTS | I |
| 3 | F | 52 | 12 | Left | Non-specific | mild FCD | I |
| 4* | F | 26 | 20 | Right | Tuberous Sclerosis | Cortical tubers | II |
| 5 | F | 22 | 15 | Right | R. MTS | MTS | II |
| 6 | M | 20 | 3 | Left | L. MTS | MTS | II |
| 7* | M | 19 | 5 | Right | Normal | Gliososis | II |

Table 1: Summary of demographics and clinical data, including MRI and histopathological findings, for the seven recruited patients in the study. Registration was performed on both hippocampus and neocortex specimens for all patients. In two cases (denoted by \star) registration was only performed on the neocortex due to a missed scan and a fragmented hippocampus specimen. MTS: Mesial Temporal Sclerosis. FCD : focal cortical dysplasia.

Specimen imaging was performed on a 3T Discovery MR750 scanner (GE Medical Systems, Milwaukee, WI, U.S.A.). Initially, an in-house developed gradient-insert coil was employed in the scanning setup with each specimen imaged sequentially using different coils. For improved time-efficiency in scanning and setup, the gradient-insert coil was not employed in later studies, and both specimens were imaged in the same field of view. Post-fixation T2-weighted scans were used in the subsequent image processing and registration. Both scanning protocols are described in detail below:

2.2.1. Scan Protocol I

The first protocol utilized a gradient-insert with a 4 channel TORO coil for the neocortex and a solenoid coil for the hippocampus, with each specimen scanned sequentially. T2-weighted images with a multi-phase balanced SSFP FIESTA sequence with 4 cycled phases were acquired for the neocortex (TR=3.5ms, TE=1.75ms, flip angle=40°, N=4, matrix=200 × 200, slice thickness=0.3, FOV=60mm) and the hippocampus (TR=3.97ms, TE=1.98ms, flip angle=40°, N=4, matrix=200 × 200, slice thickness=0.3, FOV=60mm).

2.3. Scan Protocol II

For the second protocol, a 6 channel coil, designed to image the carotid artery, was used instead of the gradient-insert coil of the previous configuration. Similar T2-weighted FIESTA images (TR=8.17ms, TE=4.08ms, flip angle=40°, N=2, matrix=200 × 200, slice thickness=0.4, FOV=120mm) with a resolution of 0.35 × 0.35 × 0.4mm, as well as, Fast gradient echo (fastGRE) scans with sixteen echoes (TR=65.0ms,

123 TE=38.9ms, flip angle=40°, matrix=200 × 200, slice thickness=0.4, FOV=120 mm) were acquired for the
124 study. A switch was made to the second protocol due to the significant time savings achieved during the
125 setup and gradient shimming processes (from ~45 min to ~5 min) and minimal loss of image resolution.

126 2.4. *Histological processing*

127 Following pre-fixation and post-fixation MRI imaging, the specimens underwent accessioning and grossing
128 at the Department of Pathology at UH, and were then cut into two halves midway, anterior-posterior, through
129 the specimen. Each half of the specimen was then embedded in agar for a stabilization effect during slicing.
130 The half-specimens were then sectioned parallel to the initial cut, into 4.4 mm pieces in the anterior to
131 posterior direction using a deli slicer (Globe Food Equipment Company, Dayton, OH, U.S.A). Each block
132 was embedded in paraffin and mounted on a microtome where 8 μm thick sections were cut from the face of
133 each block and mounted on slides. One slide from each block was stained with hematoxylin and eosin (H&E)
134 according to standard clinical neuropathology protocols, and additional stains or immunohistochemistry,
135 including glial fibrillary acidic protein (GFAP), neuronal nuclei (NeuN) and neurofilament (NF), were ordered
136 where deemed necessary by the neuropathologist on duty. The resulting slides were digitized on a ScanScope
137 GL (Aperio Technologies, Vista, CA, USA) bright field slide scanning system at a maximum of 20x optical
138 zoom, and stitched to form full-frame multi-resolution images stored in BigTIFF file format (maximum pixel
139 resolution 0.5μm). Since each specimen was sectioned into blocks of 4.4mm thickness, the corresponding
140 H&E stained images have a physical spacing of effectively 4.4mm in the coronal (anterior-posterior) direction.
141 Figure 2 shows an overview of all these histological processing steps.

142 2.5. *Image registration*

143 To motivate our registration approach we first describe how the numerous physical processing steps
144 between *ex-vivo* MR imaging and slide digitization affect the specimen, and how these steps could be
145 accounted for with registration. As outlined in the previous section, after imaging, the tissue specimen is
146 sectioned coronally, but this slicing plane is not enforced to be along the orthogonal axes corresponding to
147 the MRI coordinate system. We therefore need to obtain a transformation between the MRI axes and tissue
148 slicing axes. Next, when the specimen is mounted on the microtome, there may be variability in the angle at
149 which sections are taken and in the number of partial sections removed before a full section is retained. This
150 effectively leads to variability in the angle and spacing between sections. For similar procedures carried out
151 on prostate specimens, Gibson et al. (2012) quantified the variability to be $1.7 \pm 1.1^\circ$ and 1.0 ± 0.5 mm in
152 angle and spacing respectively. Because of the relatively small magnitude of variability, and ease of working
153 with parallel sections, we do not explicitly account for this and instead assume sections are parallel and
154 spaced by 4.4mm. The tissue being sectioned in the microtome is highly folded after the blade is brought
155 down, thus to mount the section on a slide, it is first placed in a water bath to unfold, then eased onto

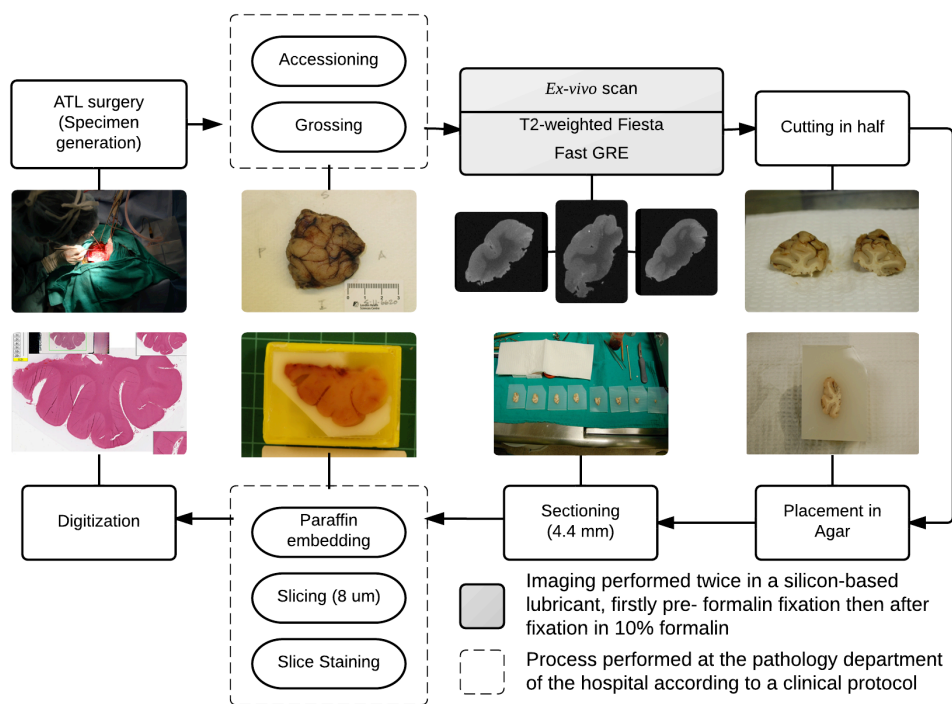


Figure 2: Overview of histological processing from specimen generation to digitization. Processes performed in a standard clinical workflow at the hospital are included in dashed boxes.

156 the glass slide. This procedure can introduce folds or tears in the mounted section, and placement on the
157 slide is variable. Histological processing and staining of the section can introduce further distortions, such
158 as differential shrinkage or expansion of tissue. Since all these deformations are present in the thin ($8\mu\text{m}$)
159 section of tissue mounted on the slide, these can be modelled as transformations and warps constrained to
160 the 2D plane.

161 In summary, we require a registration approach that can model: 1) the transformation between the 3D
162 MRI axes to the specimen slicing axes (3D rigid transformation), and 2) the transformations and deforma-
163 tions of each slide-mounted section constrained to the 2D space of the slide (2D rigid transformations and
164 non-rigid deformations).

165 *2.6. Iterative registration algorithm*

166 In this section we outline our iterative registration approach to attain the transformations and deforma-
167 tions and to establish correspondence between the MRI and histology images. Note that the registration
168 procedures for hippocampus and neocortex images were carried out separately in each case. Preliminary
169 results for neocortex registration were shown in Goubran et al. (2012).

170 If a 3D reconstruction of the histology were given, 3D rigid image registration could be used to align the
171 MRI to the histology. However, to generate a 3D reconstruction of the histology, the individual histology
172 slices would need to be corrected, using the registered MRI as a reference. Thus we see that obtaining the
173 3D rigid transformation is dependent on having a 3D histology reconstruction, and this is in turn dependent
174 on the 2D histology registration with the MRI for a reference. To resolve this circularity, we propose
175 an iterative registration scheme that alternates between 1) finding the 3D rigid transformations given the
176 current histology reconstruction, and 2) finding the 2D rigid transformations and non-rigid deformations to
177 reconstruct the histology volume given the current 3D rigid transformations.

178 Figure 3 presents a block diagram overview of our overall registration algorithm. First, the histology
179 and MRI images are pre-processed separately to obtain image pairs of the same resolution and field of
180 view suitable for image registration. Then the images are fed into an iterative registration algorithm that
181 alternates between registration of the MRI volume to the current estimate of the histology volume (3D
182 Rigid Registration), and registration of the histology slides to the reference MRI slides for histology volume
183 reconstruction (2D Rigid Registration and 2D Non-rigid Registration). The details of this registration are
184 shown in Algorithm 1.

185 *2.6.1. MR image pre-processing*

186 Prior to image registration, the images underwent a series of pre-processing steps, carried out with
187 command-line tools from the FSL image analysis suite (FSL, <http://fsl.fmrib.ox.ac.uk>) and scripts
188 written in MATLAB (The MathWorks Inc., Natick, MA, USA). First, *ex-vivo* MRI images scanned with

Input: Histology and MRI volumes: $\mathbf{H}^0 = \{H_j\}_{j=1\dots N}$, \mathbf{M}

Output: Final volume and transformations: $\mathbf{H}^{i_{max}}$, $T_{3D}^{i_{max}}$, $T_{2D,j=1\dots N}^{i_{max}}$, $\Phi_{2D,j=1\dots N}^{i_{max}}$

```

for  $i = 0$  to  $i_{max}$  do
  // 3D rigid registration between histology and MRI volume:
   $T_{3D}^i = \text{RigidReg3D}(\mathbf{H}^i, \mathbf{M})$ 
  // Transformed MRI volume:
   $\mathbf{M}^{T^i} = T_{3D}^i \circ \mathbf{M}$ 
  // For each histology slice:
  for  $j = 1$  to  $N$  do
    // 2D rigid registration between histology and MRI slice:
     $T_{2D,j}^i = \text{RigidReg2D}(M_j^{T^i}, H_j^i)$ 
    if  $i > 2$  then
      // 2D non-rigid registration between histology and MRI slice:
       $\Phi_{2D,j}^i = \text{NonRigidReg2D}(M_j^{T^i}, T_{2D,j}^i \circ H_j^i)$ ;
    else
       $\Phi_{2D,j}^i = Id$ ;
    end
    // Deformed histology slice
     $H_j^{i+1} = \Phi_{2D,j}^i \circ T_{2D,j}^i \circ H_j^i$ ;
  end
  // Updated histology volume
   $\mathbf{H}^{i+1} = \{H_j^{i+1}\}_{j=1\dots N}$ ;
end

```

Algorithm 1: Iterative 3D and 2D registration of input histology volume $\mathbf{H}^0 = \{H_j\}_{j=1\dots N}$ and MRI volume \mathbf{M} . Here, we represent image volumes in boldface (\mathbf{H}) and the corresponding slices with subscripts (H_j). In the first part of each iteration, 3D registration is carried out on the current estimate of the histology volume and the MRI volume to obtain the transformation between the MRI axes to the specimen slicing axes. In the second part, 2D registration is carried out to obtain the transformations and deformations of each slide-mounted histology section using the current estimate of the aligned reference MRI.

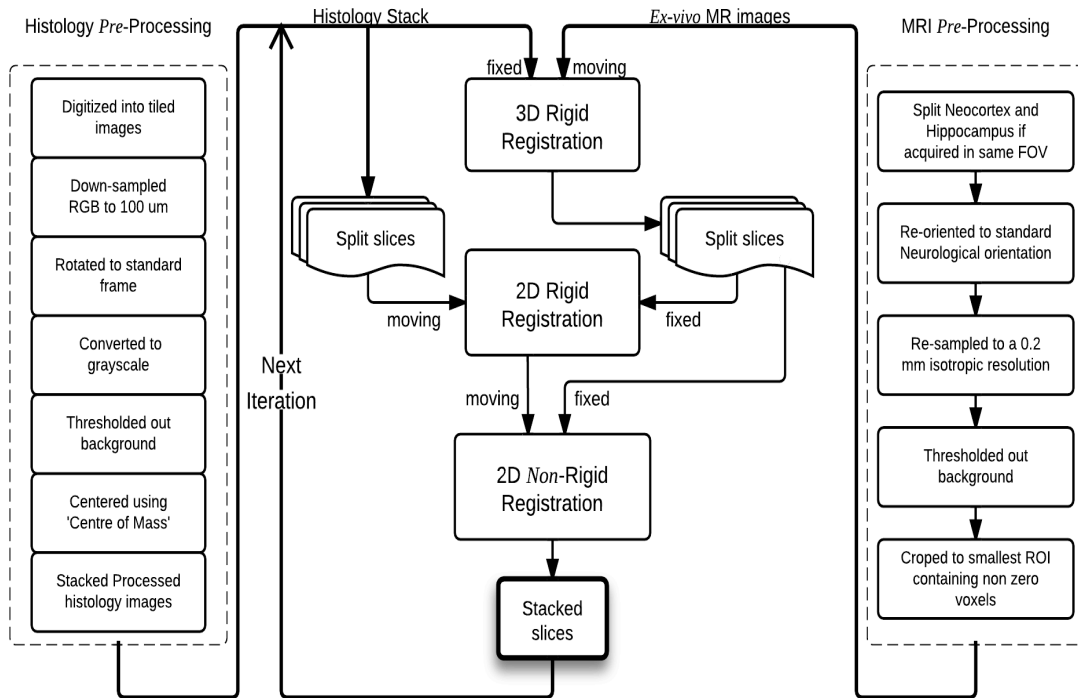


Figure 3: Registration pipeline showing pre-processing steps of the data and our iterative 2D-3D approach. The left column demonstrates the pre-processing steps applied to the histology slides sequentially from top to bottom. Likewise, the right column represents the pre-processing steps applied to the MRI of the specimens. The resulting histology stack acts as a fixed image to transform the MR image in a 3D rigid registration. The transformed image as well as the stack are split into slices 4.4 mm apart where each histology slice has a corresponding MRI slice. These MR slices act as fixed images to deform the histology slices rigidly then non-rigidly. The resulting deformed histology slices are stacked and fed back into the 3D rigid registration for the next iteration.

189 *Scan Setup II*, containing both neocortex and hippocampus specimens in the same field of view, were
190 converted from the scanner output Dicom (dcm) format to the standard Nifti (nii) format, then bisected to
191 produce separate volumes. Since the orientation of these specimens in the scanner bore did not correspond
192 to the anatomical orientation, the orientation matrices of the images volumes were updated to reflect the
193 correct pose. This operation was performed using photographs of the annotated specimens and 3D models of
194 *ex-vivo* images, and the resulting orientation matrices were applied to all the acquired images in the session.
195 The images were then background masked using a percentile threshold, resampled to 0.2 mm isotropic
196 resolution, and cropped around the perimeter of the specimen.

197 *2.6.2. Histology image pre-processing*

198 The digitized histology images were similarly reoriented into a standard orientation, with the origin
199 in the top-left image corner corresponding to superior-right in anatomical orientation, using the Aperio
200 ImageScope software (Aperio Technologies, Vista, CA, USA) and the corresponding MRI as a reference.
201 The images were then down-sampled to 100 μm in-plane resolution and converted into NIFTI format, where
202 each RGB channel was represented as a slice in a 3D volume. We converted the images to grayscale by
203 extracting the green channel, since this channel was found to possess the best gray/white matter contrast
204 in the H&E stained slides. Finally, the images were background masked and centered in a standard 60mm
205 field of view using the image-based center-of-mass in each slide.

206 *2.6.3. Rigid registration*

207 Rigid registration in our iterative scheme was carried out with the *flirt* tool from (Jenkinson and Smith,
208 2001) (FSL, <http://fsl.fmrib.ox.ac.uk/flirt>) to perform the 3D and 2D registration. The default
209 multi-modal cost function (correlation ratio) was applied and the registration was constrained to a rigid
210 transform model with 6 and 3 degrees of freedom respectively for the 3D and 2D steps.

211 *2.6.4. Non-rigid registration*

212 A deformable registration between corresponding histology and MRI slices was employed to account for
213 any anisotropic tissue deformations that can occur during histological processing, sectioning, and staining.
214 We used a fast non-rigid registration that makes use of a B-spline deformation field and a normalized mutual
215 information cost-function (Rueckert et al., 1999; Modat et al., 2010) (NiftyReg, [http://sourceforge.net/
216 projects/niftyreg/](http://sourceforge.net/projects/niftyreg/)). The B-spline image registration used a three-level multi-resolution image pyramid
217 with final control point spacing of 2 mm. Non-rigid registration was carried out starting at iteration 3 of
218 the algorithm and not having been employed in the first two iterations to ensure the sufficient convergence
219 of the rigid registration step. Furthermore, for slices where foreground of the MRI image or histology image
220 were below a specified threshold, non-rigid registration was not performed and a zero deformation was
221 assumed for the slice. The deformation penalty term (bending energy of the spline at a control point), was

222 successively relaxed after each iteration to allow for greater deformations as the alignment is improved over
223 each iteration. Specifically the sequence of bending energies employed at the iterative registration steps were
224 $\{0.5, 0.025, 0.01\}$, for iterations 3-5.

225 Due to histology tissue breakage and loss, a final registration step was added where binary ‘ignore’
226 masks defined on the registered histology slices were included in the deformable registration scheme. These
227 ignore masks were manually-defined in 3D Slicer (<http://www.slicer.org>) using a large 2 mm radius
228 paintbrush on regions of the MRI image where tissue loss is readily apparent in corresponding regions of
229 the histology image, preventing these regions from contributing to the registration, which would result in
230 incorrect deformations since one-to-one tissue correspondence is unattainable.

231 2.7. Registration validation

232 2.7.1. Landmark-based validation

233 To validate our registration protocol, we computed target registration error (TRE) based on manually-
234 identified corresponding intrinsic landmarks on MR images and histology slices. These landmarks were used
235 as independent targets to assess the accuracy of the registration at each iteration of the iterative registration
236 scheme, as well as after deformable warping of the images.

237 We found that micro-vasculature or micro-bleeds that were visible on the H&E histology slides appeared
238 as dark hypo-intense regions in the *ex-vivo* T2-weighted MRI, as demonstrated in Figure 4. First, one rater
239 identified landmarks on histology slides (downsampled to $10\mu\text{m}$ per pixel), restricting selection to vasculature
240 with a transverse diameter of more than 35 pixels wide, assuming an ellipsoid shape. The most anterior and
241 posterior histology slices in many cases of both specimens did not contain sufficient intact tissue for reliable
242 placement of anatomical landmarks. Three raters then independently searched through the *ex-vivo* MRI to
243 locate corresponding landmarks in the MRI images representing the centroid of these micro-vasculature or
244 micro-bleeds. Since tissue contrast varies throughout the specimen, other MR scans of the specimen were
245 used to facilitate the localization process. To compute the TRE the coordinates for all three raters were
246 averaged to generate a consensus set of MRI landmarks. A total of 215 pairs of corresponding landmarks
247 were identified for the TRE calculations in the twelve specimens. Note that only a single set of the histology
248 landmarks were used to ensure consistent landmark locations.

249 2.7.2. Localization error and statistical analysis

250 Target localization incorporates human error in localizing the coordinates which combines with the image
251 registration error to produce the TRE measurements. The target localization error (TLE) was calculated
252 on *ex-vivo* MRI images as an unbiased estimator of the standard deviation of repeated localizations of the
253 same landmark by the same rater (Fitzpatrick et al., 1998), described by the equation below:

$$TLE = \sqrt{\frac{1}{J} \sum_{j=1}^J \frac{1}{K-1} \sum_{K=1}^K \|P_{j,k} - \frac{1}{K} \sum_{k=1}^K P_{j,k}\|^2}$$

254 where $P_{j,k}$ is the k -th localization of the j -th landmark. A total of five localization ($K = 5$) of twenty
 255 landmarks ($J = 20$) was performed.

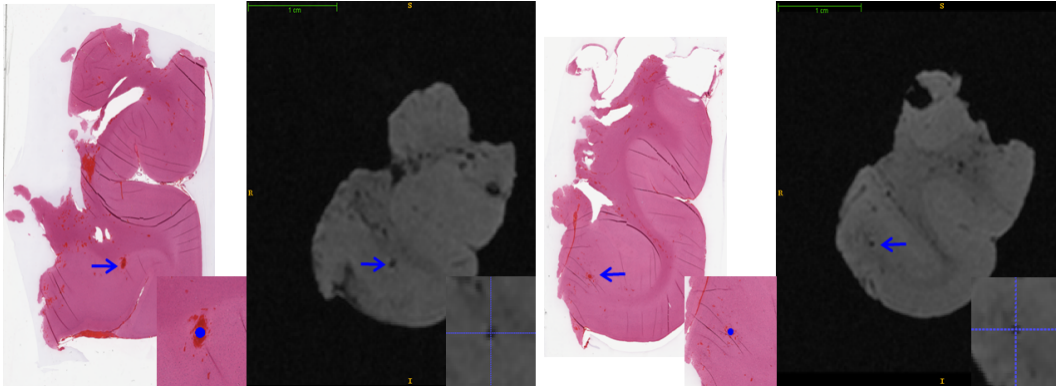


Figure 4: Preview of chosen intrinsic landmarks on histology and their localized corresponding landmark on Ex MRI. The arrows in blue pinpoint the micro vasculature used as targets for the TLE calculations on both histology and MRI. A zoomed in window demonstrates the targets on both modalities with cross hairs indicating the target coordinates on MRI and a circle showing the chosen coordinates on histology.

256 Inter-rater variability was measured as an estimator of the standard of deviation of repeated localization
 257 of the same landmarks by different raters, where a hundred and twenty eight landmarks ($J = 128$) were
 258 placed by three different raters ($K = 3$). Statistical analyses were performed in Prism 5.04 (GraphPad
 259 Software, San Diego, CA). To assess for significant differences between the several iterations of the algorithm
 260 and across rigid and non-rigid steps, we computed a repeated-measures analysis of variance (ANOVA) of the
 261 mean TRE value of each of these steps followed by Bonferroni multiple-comparison correction. A Bartlett's
 262 test for equal variances was conducted between all iterations (rigid and non-rigid) of the algorithm to verify
 263 the equal variance assumption of the ANOVA tests.

264 3. Results

265 The proposed methodology required ~ 85 min (including setup) for *ex-vivo* imaging and < 10 min for
 266 execution of both the rigid and non rigid components of the algorithm (excluding the manual re-orientation
 267 step in the pre-processing scheme and the time for definition of ignore masks). Evaluation of the protocol
 268 was performed by localization of micro vasculature landmarks seen on both modalities by three raters. The
 269 localization protocol yielded 2-4 homologous landmarks on each of 8-12 sections per neocortex specimen and
 270 1-3 landmarks on each of 6-8 sections per hippocampus specimen. Our registration protocol produced a

271 mean target registration error of 0.76 ± 0.66 for hippocampal specimens, as shown in table 2, and 0.98 ± 0.60
272 for neocortical specimens. The mean TRE was below 1.2 mm after the last step of the registration algorithm
273 in all cases including both specimens. The mean landmark localization error for the three raters was found
274 to be 0.21 mm, relative to an MRI voxel size of $0.35 \times 0.35 \times 0.4$ mm. The inter-rater reliability between the
275 raters was found to be 0.33 mm. Figure 5 shows the registration errors across all steps of the algorithm
276 including both rigid and non-rigid components for both specimens. The errors are shown first along iterations
277 1, 3 and 5 of the rigid component then the non-rigid steps beginning with a step using a high bending energy
278 regularization penalty; then a low penalty weight and finally deformable registration utilizing ignore masks,
279 that account for tissue breakage and differential shrinkage. The mean error of the rigid iterations reaches a
280 plateau around iteration 5 for both specimens. The masked imaged based step outperformed the non-masked
281 registration as expected by avoiding tissue breakage.

282 Figure 6 shows three neocortical slices with their corresponding MRI slices, that represents the loca-
283 tion where the histology cuts were made with respect to the MRI scans of the resections, as well as the
284 transformations of the slices after deformable registration. A picture of the resected specimen along with a
285 volume rendering demonstrating the location of these histology slices in respect to the whole specimen are
286 also shown in the figure. Checkerboard images of both rigid and non-rigid registration for a hippocampal
287 slice are displayed in figure 7, which also shows a rendered representation of both sides of the hippocampus
288 where the histology slice was cut.

289 The Bartlett's test confirmed the validity of the equal variance assumption for the ANOVA analyses of
290 both specimens ($P > 0.05$). The significant results of the ANOVA analysis are shown in the 'Mean' row of
291 tables 2 and 3. The ANOVA analysis, between the first deformable registration step (High Bending Energy)
292 and the last rigid step (Iteration 5), failed to show a statistically significant difference of the mean TREs
293 for both the hippocampus ($P > 0.05$, 95 % Confidence Interval [CI] of difference -0.2666 to 1.653) and
294 neocortex ($P > 0.05$, 95 % CI -0.0147 to 1.54). However, this test did demonstrate a significant decrease
295 in TRE between (High Bending Energy) and the first rigid iteration (Iteration 1) for the hippocampus and
296 neocortex respectively ($P \leq 0.01$, 95 % CI 0.143 to 1.69 and $P \leq 0.05$, 95 % CI -0.2040 to 1.715). In
297 comparison, decreasing the bending energy weight penalty produced significantly lower mean TRE than the
298 final rigid iteration step (Iteration 5) for the hippocampus and neocortex respectively ($P \leq 0.001$, 95 %
299 CI 0.449 to 2.00 and $P \leq 0.01$, 95 % CI 0.3516 to 2.271). The proposed masked non-rigid scheme (Masked
300 NR) had as well significantly lower TRE ($P \leq 0.0001$) than Iteration5 for both the hippocampus (95 % CI
301 0.590 to 2.14 mm) and neocortex (95 % CI 0.5143 - 2.434).

| | It.1 | It.3 | It.5 | H.B.E | L.B.E | Masked N.R |
|--------|-----------------|-----------------|-----------------|-------------------------|--------------------------|--------------------------|
| Subj 1 | 2.07 ± 0.96 | 2.05 ± 0.97 | 2.05 ± 0.98 | 1.35 ± 0.85 | 0.88 ± 0.67 | 0.73 ± 0.85 |
| Subj 2 | 2.81 ± 0.54 | 2.87 ± 0.63 | 2.74 ± 0.80 | 2.52 ± 0.94 | 1.42 ± 0.94 | 1.03 ± 0.94 |
| Subj 3 | 2.13 ± 1.78 | 2.12 ± 1.74 | 2.09 ± 1.73 | 1.30 ± 0.78 | 0.73 ± 0.42 | 0.62 ± 0.40 |
| Subj 4 | 2.19 ± 1.02 | 2.09 ± 1.02 | 2.07 ± 1.21 | 1.01 ± 0.54 | 0.68 ± 0.37 | 0.68 ± 0.42 |
| Subj 5 | 2.05 ± 0.84 | 1.86 ± 0.85 | 1.78 ± 0.95 | 1.15 ± 0.68 | 0.75 ± 0.43 | 0.72 ± 0.45 |
| Mean | 2.25 ± 1.10 | 2.18 ± 1.11 | 2.15 ± 1.14 | $1.46 \pm 0.77^\dagger$ | $0.89 \pm 0.61^\ddagger$ | $0.76 \pm 0.66^\ddagger$ |

Table 2: TRE values for hippocampal registration across iterations. H.B.E: Non-rigid with a High Bending Energy penalty, L.B.E: Non-rigid with a Low Bending Energy penalty. \dagger : $P \leq 0.01$ between means registration step and Rigid Iteration 1. \ddagger : $P \leq 0.01$ between means of registration step and Rigid Iteration 5.

| | It.1 | It.3 | It.5 | H.B.E | L.B.E | Masked N.R |
|--------|-----------------|-----------------|-----------------|-------------------------|--------------------------|--------------------------|
| Subj 1 | 2.97 ± 0.86 | 2.98 ± 0.86 | 2.96 ± 0.87 | 1.55 ± 1.21 | 1.26 ± 0.66 | 1.08 ± 0.52 |
| Subj 2 | 2.36 ± 0.83 | 1.92 ± 0.84 | 1.91 ± 0.94 | 1.69 ± 1.17 | 0.83 ± 0.85 | 0.72 ± 0.68 |
| Subj 3 | 2.23 ± 1.40 | 2.08 ± 1.37 | 2.07 ± 1.37 | 1.15 ± 1.15 | 0.98 ± 0.99 | 0.83 ± 0.70 |
| Subj 4 | 2.41 ± 1.61 | 2.40 ± 1.76 | 2.38 ± 1.89 | 2.17 ± 0.88 | 1.17 ± 0.68 | 1.05 ± 0.65 |
| Subj 5 | 2.19 ± 1.02 | 2.08 ± 1.02 | 2.06 ± 1.01 | 1.01 ± 0.43 | 1.02 ± 0.45 | 0.87 ± 0.38 |
| Subj 6 | 2.23 ± 1.63 | 2.24 ± 1.65 | 2.25 ± 1.65 | 2.06 ± 0.61 | 1.35 ± 0.57 | 1.12 ± 0.52 |
| Subj 7 | 2.16 ± 1.41 | 2.14 ± 1.44 | 2.11 ± 1.44 | 1.42 ± 0.55 | 1.15 ± 0.49 | 1.15 ± 0.35 |
| Mean | 2.37 ± 1.19 | 2.26 ± 1.22 | 2.25 ± 1.28 | $1.60 \pm 1.01^\dagger$ | $1.11 \pm 0.75^\ddagger$ | $0.98 \pm 0.60^\ddagger$ |

Table 3: TRE values for neocortical registration across iterations.H.B.E: Non-rigid with a High Bending Energy penalty,L. B.E: Non-rigid with a Low Bending Energy penalty. \dagger : $P \leq 0.01$ between means registration step and Rigid Iteration 1. \ddagger : $P \leq 0.01$ between means of registration step and Rigid Iteration 5.

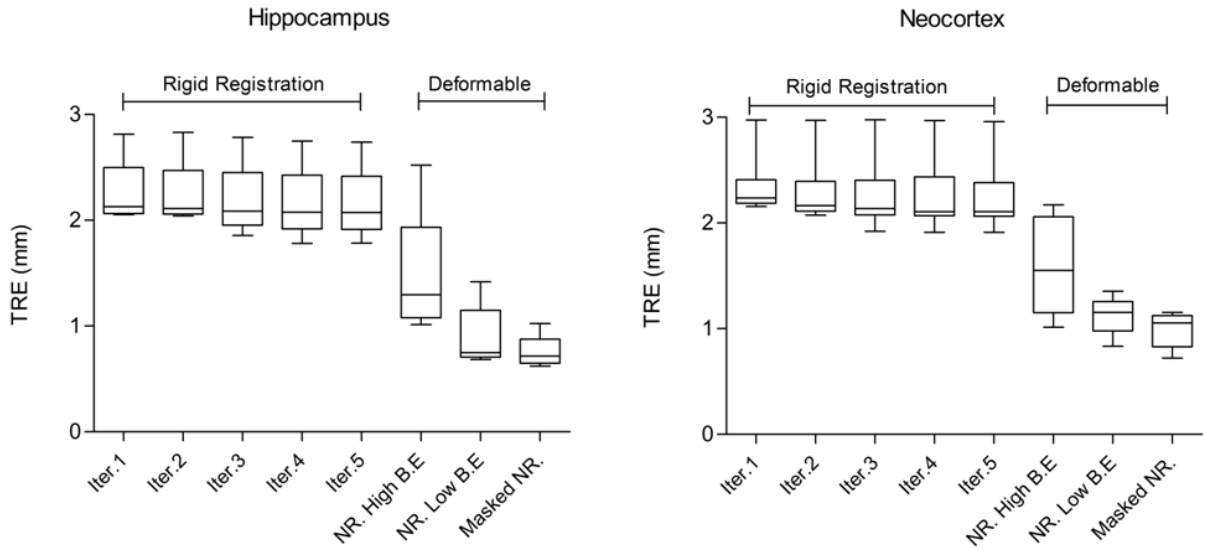


Figure 5: Boxplots with 5-95% whiskers of Hippocampal and Neocortical registration target registration errors at each stage of the iterative registration scheme.

302 4. Discussion

303 In this article, we have described a method to reliably register *ex-vivo* MRI and sparsely sliced histology
 304 slides of neocortex and hippocampus specimens. Our protocol is a landmark free algorithm that produced
 305 sub-millimeter accuracy for hippocampal registration and close to 1-mm of error for temporal lobe neocortical
 306 registration. Correlating MRI with histopathology is imperative in the validation of new imaging sequences,
 307 since verification of pathological anomalies underlying signal changes is needed to enable these sequences to
 308 ultimately gain clinical acceptance. The intrinsic higher resolution of *ex-vivo* MR images provides a superior
 309 opportunity to further examine the correlation between MRI and histology. By addressing many challenges of
 310 the in-vivo MRI to histology registration, our protocol leaves single modality registration between specimen
 311 and preoperative MRI scans as the remaining step. In addition, *ex-vivo* to MRI registration can be used to
 312 validate specimen imaging, as it has been shown by Madabhushi et al. (2005) in prostate *ex-vivo* imaging
 313 examples. While using an intermediate ex vivo registration interrupts the clinical flow for specimen imaging,
 314 our algorithm requires ~ 9 min ± 37 seconds on average (for the automated iterative 3D/2D rigid approach
 315 plus the non-rigid steps) to register $100 \mu\text{m}$ coronally sliced (anterior to posterior) histology slices to *ex-vivo*
 316 MRI images.

317 Previous studies on registration of histopathology to *in-vivo* imaging were reported mostly for rodents
 318 (Jacobs et al., 1999; Humm et al., 2003; Meyer et al., 2006; Lebenberg et al., 2010) and primates (Malandain

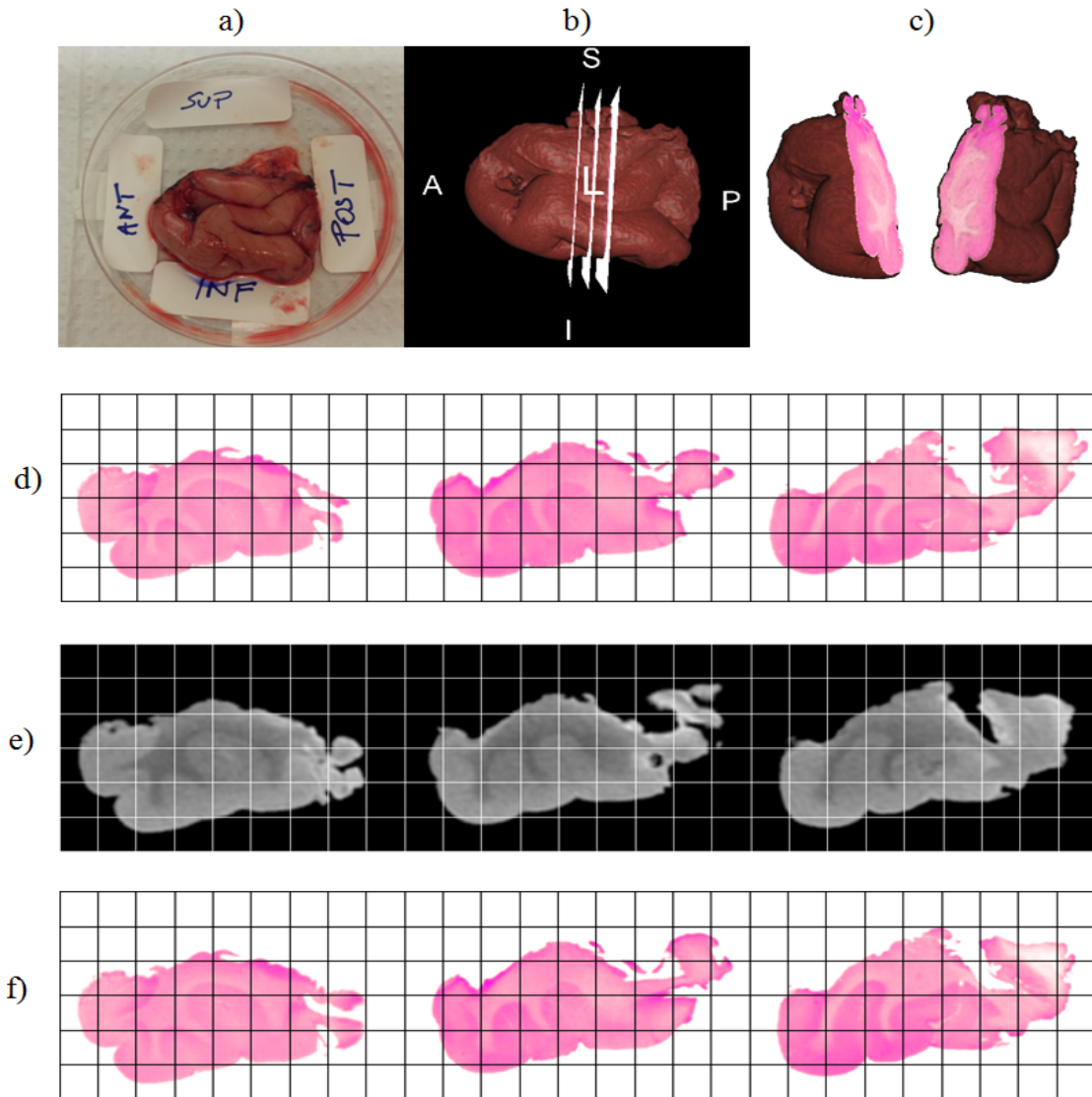


Figure 6: Example of a neocortex rigid and deformable registration showing: a) photograph of a neocortical specimen after resected with orientation labels placed by the operating surgeon, b) volume rendering of the MRI of the specimen showing the location of three consecutive histology slices. c) rendering of both sides of the specimen where the middle slice of histology was cut, d) the three histology slices shown in b), e) the corresponding MRI slices after 3D rigid registration, and f) the deformed histology slices after non-rigid registration to their corresponding MRI slices.

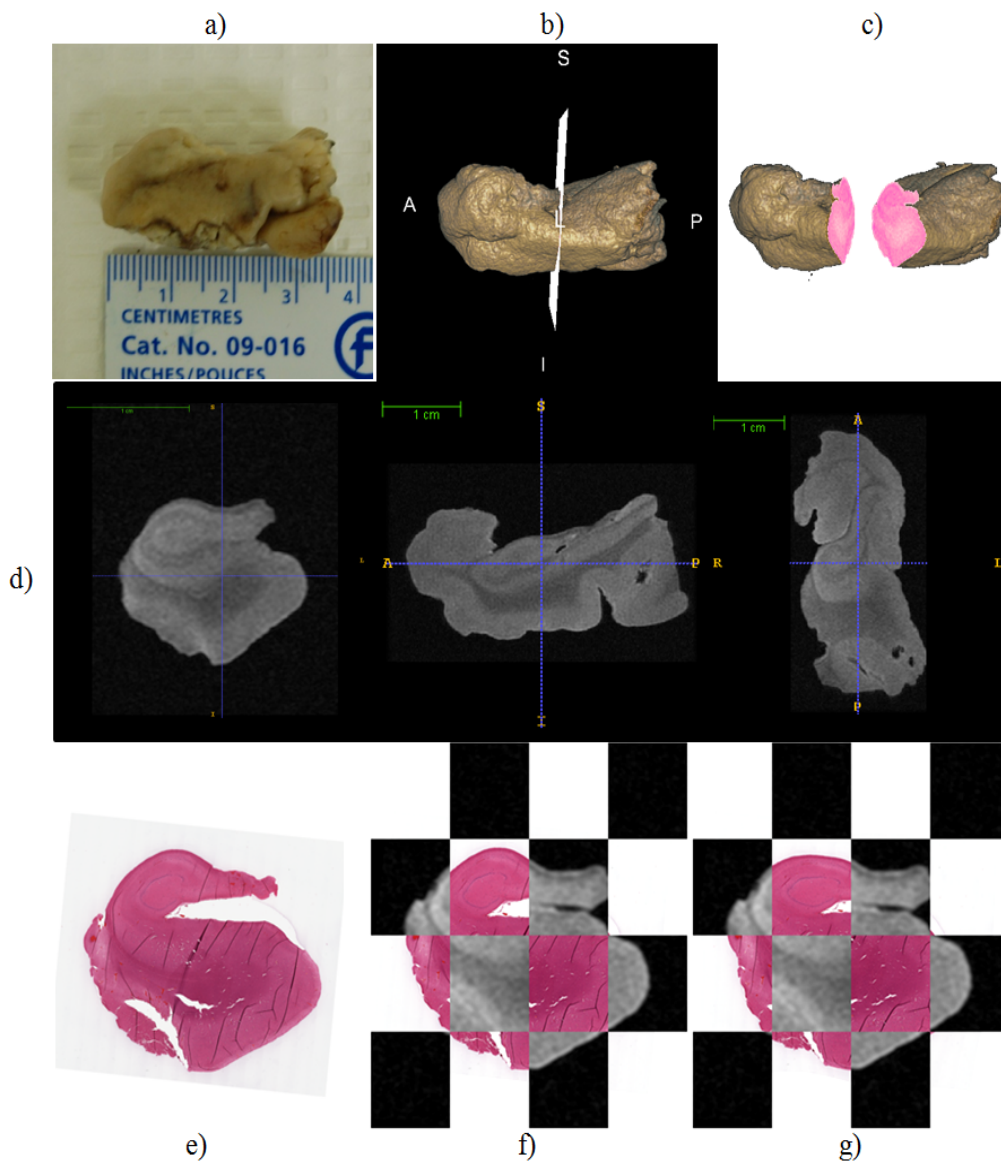


Figure 7: Example of a hippocampal rigid and deformable registration showing: a) photograph of a hippocampus before grossing, b) volume rendering of the MRI of the hippocampus demonstrating the location of a histology slice through the specimen, c) rendering of both sides of the hippocampus where the histology slice was cut, and d) three orthogonal views of the hippocampal MRI (left to right: coronal, sagittal, axial). The bottom row depicts: e) a coronal view of the same histological slice, f) a checkerboard image showing the MRI and histology before non-rigid registration, and g) a checkerboard image showing the MRI and non-rigidly deformed histology slice.

319 et al., 2004; Breen et al., 2005; Dauguet et al., 2007; Ceritoglu et al., 2010). Relatively few studies were
320 developed to register human whole-brain or single hemisphere postmortem MRI with histology (Schormann
321 et al., 1995; Kim et al., 2000; Singh et al., 2008). These landmark-based and image-based registration
322 algorithms, however, are not likely to be applicable to the registration of specimens from lobectomies to
323 full preoperative MR images, due to the drastic change in shape and coherence when the specimen is
324 separated from neighbouring tissue. Several previous works reconstructed a 3D histology volume from
325 serially sectioned brain specimens at $< 700\mu\text{m}$ to register to the MRI volume (Bardinet et al., 2002; Humm
326 et al., 2003; Dauguet et al., 2007; Lebenberg et al., 2010; Chakravarty et al., 2006). This technique while
327 producing accurate results is not compatible with the clinical work flow of pathology departments, where the
328 tissue is sparsely sectioned at a thickness of more than a few mm. Other methods have been proposed that
329 allow co-registration of histology to other modalities through the use of stereotactic systems using target
330 points (Schmierer et al., 2003; Humm et al., 2003), however the design of these systems is tissue-specific and
331 is not broadly applicable to other brain resections.

332 The measurement of TRE requires the identification of homologous landmarks on images of both modalities
333 used for registration and is frequently lacking in analyses of these methods. A few articles have quantified
334 and reported TRE in brain histology to MRI. Jacobs et al. (1999) reported a registration residual root-mean
335 square (RMS) error of 0.83 mm between histological sections and MRI of ischemic rats and Humm et al.
336 (2003) obtained a 0.25 mm registration error for tumor xenografts of one mice using stereotactic fiducial
337 markers. Both studies could not be extrapolated or compared to human cases due to the methodological
338 differences between these protocols and resected human specimens, as well as the mechanical differences
339 between excised human and whole primate brain. Singh et al. (2008) reported a 5.1 mm TRE computed as
340 3D coordinates of centroid of marked lesions in both modalities, which exceeds the desired error range for
341 correlation between histopathology and MRI in focal epilepsy as underlying pathologies may be found on the
342 scale of millimetres. Our method produced a mean TRE of 0.76 ± 0.66 and 0.98 ± 0.60 for hippocampal and
343 neocortical specimens respectively, which is sufficient for exploring underlying pathologies of focal epilepsy.
344 For a very small FCD with a volume of 128mm^3 (Besson et al., 2008), the mean TRE obtained from our
345 algorithm is able to achieve a 70% overlap of the FCD, assuming it is a sphere. Our mean TRE of 0.21 mm
346 is indicative that the localization variability is not dominating in the TRE measurements. The significantly
347 lower mean TRE for the latter deformable registration found by our ANOVA analysis motivates the use of
348 the hierarchal bending energies as well as the incorporation of ignore masks.

349 A previous method proposed visual comparison of photographs of temporal lobe neocortex tissue slices
350 to MRI, and reported a < 2 mm difference between two observers in most cases (Eriksson et al., 2005).
351 This manual matching technique suffers from a major limitation that is the lack of image registration
352 between the histology and MRI, which in turn dictates the use of region of interest (ROI) based analysis
353 in further studies of correlation (Eriksson et al., 2007, 2009; Lockwood-Estrin et al., 2012). This operator-

354 based method incorporates human bias in locating the corresponding slice of MRI, which explains the 4-mm
355 difference between raters in their last case. Only two ROIs in temporal lobe neocortical specimen were
356 assessed in Lockwood-Estrin’s and Eriksson’s work to analyze histopathology to MRI correlation. In one
357 instance a negative correlation was seen between grey matter T2 values of fast Flair (fFT2) and NeuN
358 field fraction (Eriksson et al., 2007), and another no correlation was found between normalized FLAIR
359 signal intensity (nFSI) and NeuN field fraction within these ROIs (Lockwood-Estrin et al., 2012). While
360 the differences between fFT2 and nFSI may not necessarily explain this discrepancy, averaging across the
361 whole area of the ROI may mask signal changes of pathologies smaller than the size of the ROI. Moreover,
362 unlike our protocol, Eriksson et al. (2005) focused on matching temporal lobe neocortical specimen and
363 no hippocampal correspondence was performed. Registration of the hippocampus is very challenging due
364 to the smaller size of the resection and the higher susceptibility of the tissue to deform and the histology
365 slices to break apart. Furthermore, performing an image-based registration allows exploratory hypothesis-
366 free analysis at a voxel-wise level and does not require ROI definition, which may be more sensitive to
367 subtle pathologies. Our protocol will be complemented with 3D *in-vivo* to *ex-vivo* MR registration in order
368 to explore the correlations between MRI and histology at greater depth, and provide histopathological
369 validation of multi-modal MRI analysis techniques.

370 5. Conclusion

371 We present here a protocol for registration of *ex-vivo* specimen MRI to histopathology, specifically hip-
372 pocampal and neocortical temporal lobe sections. Sub-millimeter errors have been shown for *ex-vivo* MRI to
373 histology registration on twelve collected specimens from seven patients. A successful registration between
374 histology - currently considered as the ground truth - and post-operative MRI of resected tissue is imperative
375 for better understanding of focal epilepsy at both the micro and macro levels. This correspondence is a key
376 component towards achieving MRI and histology correlation by bringing together information from both
377 domains.

378 6. Acknowledgments

379 The authors would like to thank Dr. Seyed Mirsattari, Dr. Robert Hammond and Dr. Andrew Parrent
380 for their assistance and support throughout the study. This project is funded by the Canadian Institute
381 of Health Research (CIHR) grant MOP 184807 and Canada Foundation for Innovation (CFI) grant 20994.
382 MG is supported by the NSERC Create Grant CAMI award at Western University. AK is supported by the
383 Canadian Institute of Health Research (CIHR) Fellowship.

384 **References**

- 385 Bardinet, E., Ourselin, S., Dormont, D., Malandain, G., Tandé, D., Parain, K., Ayache, N., Yelnik, J., 2002. Co-registration
386 of histological, optical and mr data of the human brain. *Medical Image Computing and Computer-Assisted Intervention—*
387 *MICCAI 2002*, 548–555.
- 388 Bernasconi, A., Bernasconi, N., Caramanos, Z., Reutens, D. C., Andermann, F., Dubeau, F., Tampieri, D., Pike, B. G., Arnold,
389 D. L., 2000. T2 relaxometry can lateralize mesial temporal lobe epilepsy in patients with normal MRI. *Neuroimage* 12 (6),
390 739–46.
- 391 Bernasconi, N., Duchesne, S., Janke, A., Lerch, J., Collins, D. L., Bernasconi, A., 2004. Whole-brain voxel-based statistical
392 analysis of gray matter and white matter in temporal lobe epilepsy. *Neuroimage* 23 (2), 717–23.
- 393 Bernhardt, B. C., Worsley, K. J., Kim, H., Evans, A. C., Bernasconi, A., Bernasconi, N., 2009. Longitudinal and cross-sectional
394 analysis of atrophy in pharmaco-resistant temporal lobe epilepsy. *Neurology* 72 (20), 1747–54.
- 395 Besson, P., Andermann, F., Dubeau, F., Bernasconi, A., 2008. Small focal cortical dysplasia lesions are located at the bottom
396 of a deep sulcus. *Brain* 131 (Pt 12), 3246–55.
- 397 Breen, M. S., Lancaster, T. L., Wilson, D. L., 2005. Correcting spatial distortion in histological images. *Comput Med Imaging*
398 *Graph* 29 (6), 405–17.
- 399 Ceritoglu, C., Wang, L., Selemon, L. D., Csernansky, J. G., Miller, M. I., Ratnanather, J. T., 2010. Large Deformation
400 Diffeomorphic Metric Mapping Registration of Reconstructed 3D Histological Section Images and in vivo MR Images. *Front*
401 *Hum Neurosci* 4, 43.
- 402 Chakravarty, M. M., Bertrand, G., Hodge, C. P., Sadikot, A. F., Collins, D. L., 2006. The creation of a brain atlas for image
403 guided neurosurgery using serial histological data. *Neuroimage* 30 (2), 359–76.
- 404 Dauguet, J., Delzescaux, T., Condé, F., Mangin, J.-F., Ayache, N., Hantraye, P., Frouin, V., 2007. Three-dimensional recon-
405 struction of stained histological slices and 3D non-linear registration with in-vivo MRI for whole baboon brain. *Journal of*
406 *neuroscience methods* 164 (1), 191–204.
- 407 de Tisi, J., Bell, G. S., Peacock, J. L., McEvoy, A. W., Harkness, W. F. J., Sander, J. W., Duncan, J. S., 2011. The long-term
408 outcome of adult epilepsy surgery, patterns of seizure remission, and relapse: a cohort study. *Lancet* 378 (9800), 1388–95.
- 409 Engel, J., 1998. Etiology as a risk factor for medically refractory epilepsy: a case for early surgical intervention. *Neurology*
410 51 (5), 1243–4.
- 411 Engel, J., Levesque, M. F., Shields, W. D., 1992. Surgical treatment of the epilepsies: presurgical evaluation. *Clin Neurosurg*
412 38, 514–34.
- 413 Eriksson, S. H., Free, S. L., Thom, M., Harkness, W., Sisodiya, S. M., Duncan, J. S., 2005. Reliable registration of preoperative
414 MRI with histopathology after temporal lobe resections. *Epilepsia* 46 (10), 1646–53.
- 415 Eriksson, S. H., Free, S. L., Thom, M., Martinian, L., Symms, M. R., Salmenpera, T. M., McEvoy, A. W., Harkness, W.,
416 Duncan, J. S., Sisodiya, S. M., 2007. Correlation of quantitative MRI and neuropathology in epilepsy surgical resection
417 specimens—T2 correlates with neuronal tissue in gray matter. *Neuroimage* 37 (1), 48–55.
- 418 Eriksson, S. H., Free, S. L., Thom, M., Symms, M. R., Martinian, L., Duncan, J. S., Sisodiya, S. M., 2009. Quantitative grey
419 matter histological measures do not correlate with grey matter probability values from in vivo MRI in the temporal lobe.
420 *Journal of neuroscience methods* 181 (1), 111–8.
- 421 Fish, D. R., Smith, S. J., Quesney, L. F., Andermann, F., Rasmussen, T., 1993. Surgical treatment of children with medically
422 intractable frontal or temporal lobe epilepsy: results and highlights of 40 years’ experience. *Epilepsia* 34 (2), 244–7.
- 423 Fitzpatrick, J. M., West, J. B., Maurer, C. R., 1998. Predicting error in rigid-body point-based registration. *IEEE Trans Med*
424 *Imaging* 17 (5), 694–702.
- 425 Gibson, E., Gómez, J., Moussa, M., Crukley, C., Bauman, G., Fenster, A., Ward, A., 2012. 3d reconstruction of prostate

426 histology based on quantified tissue cutting and deformation parameters. In: Society of Photo-Optical Instrumentation
427 Engineers (SPIE) Conference Series. Vol. 8317. p. 22.

428 Goubran, M., Khan, A. R., Crukley, C., Buchanan, S., Santyr, B., deRibaupierre, S., Peters, T. M., 2012. Robust registration
429 of sparsely sectioned histology to ex-vivo MRI of temporal lobe resections. Vol. 8314. p. 83141V.

430 Howe, K. L., Dimitri, D., Heyn, C., Kiehl, T.-R., Mikulis, D., Valiante, T., 2010. Histologically confirmed hippocampal
431 structural features revealed by 3T MR imaging: potential to increase diagnostic specificity of mesial temporal sclerosis.
432 *AJNR American journal of neuroradiology* 31 (9), 1682–9.

433 Humm, J. L., Ballon, D., Hu, Y. C., Ruan, S., Chui, C., Tulipano, P. K., Erdi, A., Koutcher, J., Zakian, K., Urano, M.,
434 Zanzonico, P., Mattis, C., Dyke, J., Chen, Y., Harrington, P., O'Donoghue, J. A., Ling, C. C., 2003. A stereotactic method for
435 the three-dimensional registration of multi-modality biologic images in animals: NMR, PET, histology, and autoradiography.
436 *Med Phys* 30 (9), 2303–14.

437 Jacobs, M. A., Windham, J. P., Soltanian-Zadeh, H., Peck, D. J., Knight, R. A., 1999. Registration and warping of magnetic
438 resonance images to histological sections. *Med Phys* 26 (8), 1568–78.

439 Jenkinson, M., Smith, S., 2001. A global optimisation method for robust affine registration of brain images. *Medical Image*
440 *Analysis* 5 (2), 143–56.

441 Kim, T., Singh, M., Sungkarat, W., Zarow, C., Chui, H., 2000. Automatic registration of postmortem brain slices to MRI
442 reference volume. *Nuclear Science, IEEE Transactions on* 47 (4), 1607–1613.

443 Lebenberg, J., Hérard, A. S., Dubois, A., Dauguet, J., Frouin, V., Dhenain, M., Hantraye, P., Delzescaux, T., 2010. Validation
444 of MRI-based 3D digital atlas registration with histological and autoradiographic volumes: An anatomofunctional transgenic
445 mouse brain imaging study. *Neuroimage* 51 (3), 1037–1046.

446 Lockwood-Estrin, G., Thom, M., Focke, N. K., Symms, M. R., Martinian, L., Sisodiya, S. M., Duncan, J. S., Eriksson, S. H.,
447 2012. Correlating 3T MRI and histopathology in patients undergoing epilepsy surgery. *Journal of Neuroscience Methods*
448 205 (1), 182–9.

449 Madabhushi, A., Feldman, M. D., Metaxas, D. N., Tomaszewski, J., Chute, D., 2005. Automated detection of prostatic
450 adenocarcinoma from high-resolution ex vivo MRI. *IEEE Transactions on Medical Imaging* 24 (12), 1611–25.

451 Malandain, G., Bardinet, E., Nelissen, K., Vanduffel, W., 2004. Fusion of autoradiographs with an MR volume using 2-D and
452 3-D linear transformations. *Neuroimage* 23 (1), 111–27.

453 Meyer, C. R., Moffat, B. A., Kuszpit, K. K., Bland, P. L., Mckeever, P. E., Johnson, T. D., Chenevert, T. L., Rehemtulla,
454 A., Ross, B. D., 2006. A methodology for registration of a histological slide and in vivo MRI volume based on optimizing
455 mutual information. *Mol Imaging* 5 (1), 16–23.

456 Modat, M., Ridgway, G. R., Taylor, Z. A., Lehmann, M., Barnes, J., Hawkes, D. J., Fox, N. C., Ourselin, S., 2010. Fast
457 free-form deformation using graphics processing units. *Computer methods and programs in biomedicine* 98 (3), 278–84.

458 Rueckert, D., Sonoda, L. I., Hayes, C., Hill, D. L., Leach, M. O., Hawkes, D. J., 1999. Nonrigid registration using free-form
459 deformations: application to breast MR images. *IEEE Transactions on Medical Imaging* 18 (8), 712–21.

460 Schmierer, K., Scaravilli, F., Barker, G. J., Gordon, R., MacManus, D. G., Miller, D. H., 2003. Stereotactic co-registration of
461 magnetic resonance imaging and histopathology in post-mortem multiple sclerosis brain. *Neuropathol Appl Neurobiol* 29 (6),
462 596–601.

463 Schormann, T., Dabringhaus, A., Zilles, K., 1995. Statistics of deformations in histology and application to improved alignment
464 with MRI. *IEEE Transactions on Medical Imaging* 14 (1), 25–35.

465 Singh, M., Rajagopalan, A., Kim, T.-S., Hwang, D., Chui, H., Zhang, X.-L., Lee, A.-Y., Zarow, C., 2008. Co-registration of
466 In-Vivo Human MRI Brain Images to Postmortem Histological Microscopic Images. *Int. J. Imaging Syst. Technol.* 18 (5-6),
467 325–335.

468 Smith, S. J. M., 2005. EEG in the diagnosis, classification, and management of patients with epilepsy. *Journal of Neurology*,

